CrossMark

Electrical characterizations of $BaZr_{0.05}Ti_{0.95}O_3$ perovskite ceramic by impedance spectroscopy, electric modulus and conductivity

G. Nag Bhargavi[1] · Ayush Khare[1] · Tanmaya Badapanda[2] · M. Shahid Anwar[3] ·
Nameeta Brahme[4]

Abstract We, here in report on the impedance, modulus and conductivity analyses of polycrystalline perovskite structured $BaZr_{0.05}Ti_{0.95}O_3$ ceramic prepared by the conventional solid state reaction technique (SSRT). The X-ray diffraction (XRD) pattern of the specimen confirms the formation of phase pure perovskite structure. The surface morphology of the sample investigated by scanning electron microscopy (SEM) reveals closed packing of grains having good density and very less porosity. Impedance spectroscopy, electric modulus and conductivity have been used as a tool to investigate the electrical conduction mechanism occurring within the material. These studies are performed as a function of both temperature and frequency. The sample has been observed to exhibit negative temperature coefficient of resistance (NTCR) behavior indicating its semiconducting character. The Cole–Cole plots indicate the presence of both grains and grain boundaries. The various relaxation times in the electric modulus studies indicate that the material does not follow Debye law. The conductivity variation of $BaZr_{0.05}Ti_{0.95}O_3$ ceramic has also been reported as a function of temperature.

1 Introduction

The lead free perovskite structured (ABO_3) ceramics have been studied extensively due to their excellent electrical properties, thermal stability and eco friendliness [1–7]. Barium titanate ($BaTiO_3$) is one such perovskite that has been investigated for its remarkable dielectric, ferroelectric, piezoelectric and pyroelectric properties in last few decades [8–11]. This electro-ceramic offers incredible applications in multi layer ceramic capacitor (MLCC), thermistors, piezoelectric sensors, transducers and electro-optic devices [12–16]. Apart from excellent electrical properties, $BaTiO_3$ suffers from certain limitations like high dielectric loss and low figure of merit. Simple substitution of Ti^{4+} ions (ionic radius 0.068 nm) by Zr^{4+} ions (ionic radius 0.087 nm) results in a new system namely barium zirconium titanate ($BaZr_xTi_{1-x}O_3$). BZT is a system, which is chemically and thermally more stable as compared to other perovskites, and possesses a good figure of merit also in the light of electrical properties. It is important to mention that the larger ionic radius of Zr^{4+} expands the lattice structure reducing conduction due to electron hopping between Ti^{4+} and Ti^{3+} ions. The BZT system with high dielectric, ferroelectric and piezoelectric properties has been an interesting material for capacitor industry applications [17–20]. The investigations on BZT solid solutions are vast due to the possibility to tailor the ferroelectric properties by controlling the composition. Small amount of Zr^{4+} ions change the temperature dependent dielectric properties from normal ferroelectric to relaxor ferroelectric [21].

$BaTiO_3$ is well known for three structural phase transitions (i) cubic to tetragonal (paraelectric to ferroelectric) at 120 °C, (ii) tetragonal to orthorhombic (ferroelectric to ferroelectric) at 5 °C and (iii) orthorhombic to rhombohedral (ferroelectric to ferroelectric) at −90 °C

✉ Ayush Khare
  akhare.phy@nitrr.ac.in

1 Department of Physics, National Institute of Technology, Raipur 492010, India

2 Nanophotonics Laboratory, Department of Physics, C.V. Raman College of Engineering, Bhubaneswar 752054, India

3 Colloids & Materials Chemistry, Institute of Minerals and Materials Technology, Bhubaneswar 751013, India

4 School of Studies in Physics and Astrophysics, Pt. Ravishankar Shukla University, Raipur 492010, India

[22–24]. The compositional dependence of various properties of BZT lays in the fact that small amount of Zr added to BaTiO$_3$ shifts the paraelectric to ferroelectric phase transition temperature towards lower side, and ferroelectric to ferroelectric phase transition towards higher side. For a composition of BZT (0.1 < x < 0.15) all the three peaks merge into a single peak, and the room temperature phase is assigned to be tetragonal. As a consequence, a diffused phase transition in permittivity versus temperature plot starts. The relaxor compositions of BZT (x > 0.15) have received considerable interest, and corresponding electrical properties are reported by many research groups [25–30]. But, a thorough survey of literature suggests that there has not been paid much attention to the normal ferroelectric compositions of BZT (x < 0.15) perhaps due to lack of commendable dielectric properties. Other than dielectric properties, promising piezoelectric properties of BZT in the range of $0.03 \leq x \leq 0.08$ have also been reported by many researchers [31–34].

Impedance spectroscopy is a powerful tool to investigate electrical conduction behavior, and the effects of grains and grain boundaries in any ceramic system [35]. This study can be expanded for a wide range of temperature and frequency. Also, the impedance plots in a complex plane resulting in the form of semicircles indicate electrical phenomenon due to the presence of grains, grain boundary effect and space charge polarization [36]. In addition to impedance analysis, the study of electrical modulus also indicates multiple relaxations, conduction process, and charge transport mechanism involved in the system. In particular, it is the most convenient method to extract information and determine conductivity relaxation times due to electrodes [37].

Method of synthesis plays a very important role in controlling the physical properties of electroceramics [38, 39]. Different methods have been employed by researchers in order to obtain single phase, homogeneous and good quality product of BZT. To achieve a quality product with respect to purity, homogeneity, reactivity, particle size, etc., each method finds its own advantages and disadvantages. In this contest, the SSRT is found to be the easier, convenient and low cost technique among other available methods by means of performance, reliability, reproducibility and economy. High temperature SSRT is a conventional method used by many researchers for synthesis of ceramics like BZT.

In the present work, we report on the structural, microstructural and conduction behavior of SSRT synthesized BaZr$_{0.05}$Ti$_{0.95}$O$_3$ perovskite type compound using impedance spectroscopy and electric modulus studies.

2 Experimental details

In the present work, the BaZr$_{0.05}$Ti$_{0.95}$O$_3$ ceramic is synthesized by high temperature SSRT. For this, high purity precursors namely BaCO$_3$ (99.9%), ZrO$_2$ (99.8%), and TiO$_2$ (99.9%) provided by Merck India are used as precursors. All the starting materials are taken in their stoichiometric proportions according to following Eq. (1) and weighed using an electronic balance. The as weighed chemicals are mixed and ground thoroughly in the presence of acetone and distilled water in an agate mortar. The grinding is done for almost 4 h until the slurry becomes dry, and we get a residue in powder form. The powder is then calcined at a temperature of 1200 °C in a high temperature programmable furnace at a heating rate of 5 °C/min for 4 h. After confirming the phase formation (perovskite) through XRD, the powder is sintered for densification. Before sintering, the powdered specimen is shaped in form of a pellet in an hydraulic press at a pressure of 200 MPa. For pelletizing, the specimen is mixed with 2 wt% polyvinyl alcohol (PVA), which acts as a binder. Then, the pellet is sintered at 1300 °C for 4 h at the same heating rate as in case of calcination. The sintered pellet is coated on both the sides with silver paste and heat treated at 700 °C for 15 min to make the surfaces conducting. After that, the electrical measurements are performed on so prepared pellet.

$$BaCO_3 + xZrO_2 + (1 - x)TiO_2 \rightarrow BaZr_xTi_{(1-x)}O_3 + CO_2 \uparrow$$

$$(1)$$
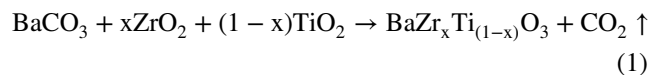
The phase uniformity, crystal structure and cell parameters of the specimen are confirmed through powder X-ray diffractometer (Philips; PW-1830) employing Cu–K$_\alpha$ (λ = 1.5418 Å) as radiation source in a wide range of 2θ (20° ≤ 2θ ≤ 90°) at a scanning rate of 2°/min. The obtained XRD peaks are analyzed using X'pert highscore plus software. To confirm the topology and morphology of the prepared specimen, scanning electron microscope (Zeiss; EVO 18) is used. The frequency and temperature dependent impedance and electrical modulus measurements are carried out using a N4L-NumetriQ frequency response analyzer (model PSM1735) connected to a computer.

3 Results and discussion

3.1 XRD analysis

The XRD pattern of BaZr$_{0.05}$Ti$_{0.95}$O$_3$ ceramic powder heat treated at 1200 °C for 4 h is shown in Fig. 1. All the XRD peaks are indexed after thorough analysis, and the pattern matches well with the JCPDS card no. 98-001-3467. The obtained peaks are sharp and highly intense
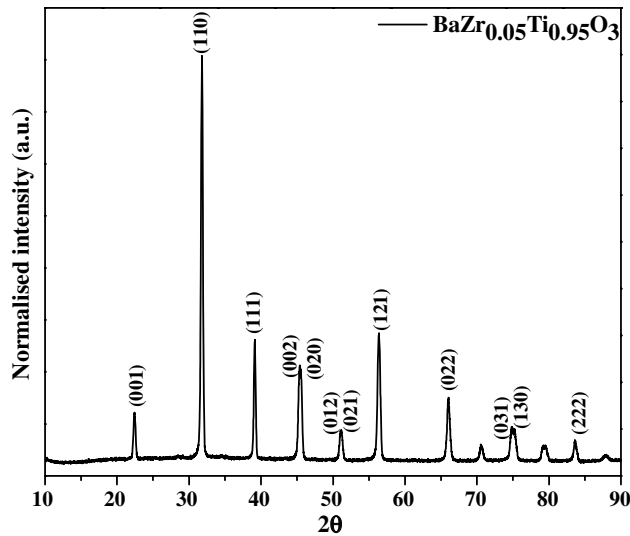
Fig. 1 XRD pattern of $BaZr_{0.05}Ti_{0.95}O_3$ ceramic calcined at 1200 °C for 4 h
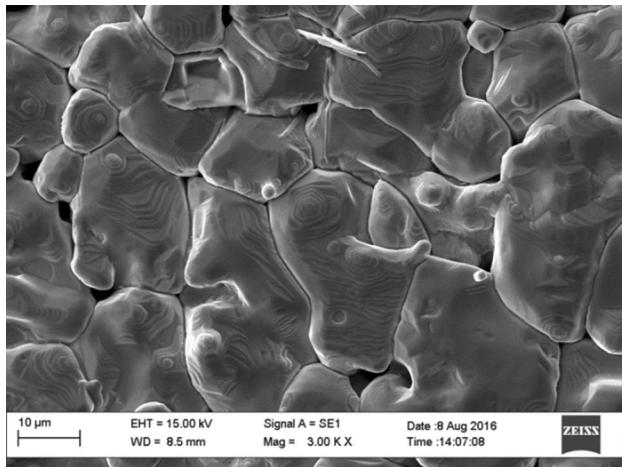
Fig. 2 SEM image of $BaZr_{0.05}Ti_{0.95}O_3$ ceramic sintered at 1300 °C for 4 h

indicating the long range crystallinity in the sample. The most intense peak is observed at 31.8° and indexed as (110). There is not witnessed presence of any deleterious phase that confirms the formation of single phase compound. The cell parameters calculated from XRD data assign orthorhombic structure (space group—Amm2) to the specimen at room temperature [22]. The calculated values of cell parameters are; $a = 3.9854$ Å, $b = 5.6713$ Å, $c = 5.6801$ Å and $\alpha = \beta = \gamma = 90°$.

3.2 SEM studies

The SEM micrograph of $BaZr_{0.05}Ti_{0.95}O_3$ pellet sintered at 1300 °C is presented in Fig. 2. The micrograph indicates closed packing of grains having good density with very less porosity. Also, the grains are well separated from each other by boundaries that are clearly visible in the micrograph. The shape of the grains is irregular and the average grain size observed is about 5–6 μm. The ferroelectric domains observed in the micrograph having lamellar structures validate the formation of sample with desired morphology [40, 41].

3.3 Complex impedance spectroscopy

The electrical properties of an electro-ceramic are largely governed by the inter-grain, intra-grain and electrode effects. A polycrystalline material (ceramic) is generally affected by both grains and grain boundaries [42]. The inter-grain boundaries in ceramics are defective regions, where deviations from oxygen stoichiometry and segregation of impurities, dopants or secondary phases could occur. Accordingly, it is expected from the electrical point of view that the grains (bulk) and grain boundary regions should have different dielectric and conductive properties [43]. Complex impedance spectroscopy is a powerful tool, which characterizes the electrical properties of a material. It is used to investigate the dynamics of bound or mobile charge in the bulk or interfacial regions of any kind of solid including ionic or mixed electronic–ionic materials and even insulators [35]. In this respect, certain parameters like complex impedance (Z*), complex modulus (M*), complex admittance (Y*), complex permittivity (ε*) and dielectric loss are important to measure. All these frequency dependent parameters are expressed by the following relationships [44]:

$$Z^*(\omega) = Z' - jZ'' = R_s - j\frac{j}{\omega c_s} = \frac{1}{j\omega c_0 \varepsilon^*} \tag{2}$$

$$M^*(\omega) = M' + jM'' = \frac{1}{\varepsilon^*} = j\omega C_0 Z^* \tag{3}$$

$$Y^*(\omega) = Y' - jY'' = \frac{1}{R_p} + j\omega C_p = j\omega C_0 \varepsilon^* = \frac{1}{Z*} \tag{4}$$

$$\varepsilon^*(\omega) = \varepsilon' - j\varepsilon'' \tag{5}$$

$$\tan\delta = \frac{Z'}{Z''} = \frac{M''}{M'} = \frac{Y'}{Y''} = \frac{\varepsilon''}{\varepsilon'} \tag{6}$$

where ω (=$2\pi f$) is angular frequency; $j = \sqrt{-1}$; R_s and R_p are the effective resistances in series and parallel respectively; C_s and C_p are resultant capacitances in series and parallel respectively; C_0 is the geometrical capacitance; Z', M', ε', Y' and Z'', M'', ε'', Y'' are real and imaginary parts of impedance, modulus, permittivity and admittance respectively.

Figure 3 shows the variation of real part (Z') of impedance with frequency at various temperatures. From the graph, it is observed that Z' decreases with increase in frequency as well as temperature, which is an indication of increase in AC conductivity with rise in temperature. From the figure, it is also observed that for all the temperatures, different Z' curves coincide at higher values of frequency. This can be attributed to the release of space charge and lowering of barrier potentials within the material [43, 45–47]. Further, it is observed that at low frequencies, Z' decreases with increasing temperature indicating negative temperature coefficient of resistance (NTCR) behavior of the sample, which is similar to the semiconductors.

Figure 4 shows the variation of imaginary part (Z'') of impedance with frequency at various temperatures. From the graph, it is observed that at lower temperatures (≤ 400 °C), Z'' initially rises, reaches the maxima (Z''_{max}) and then decreases at higher frequencies. Further, the Z''_{max} is observed to shift to higher frequencies with increasing temperatures. The decreasing magnitude of Z''_{max} with temperature indicates decrease in resistive property. The broadening of peaks with increase in temperature is another characteristic, which indicates the existence of temperature dependent electrical relaxation phenomenon of non-Debye nature in the material [48]. Again the merger of different Z'' curves at higher frequencies for all the temperatures is a sign of accumulation of space charge in the material. The
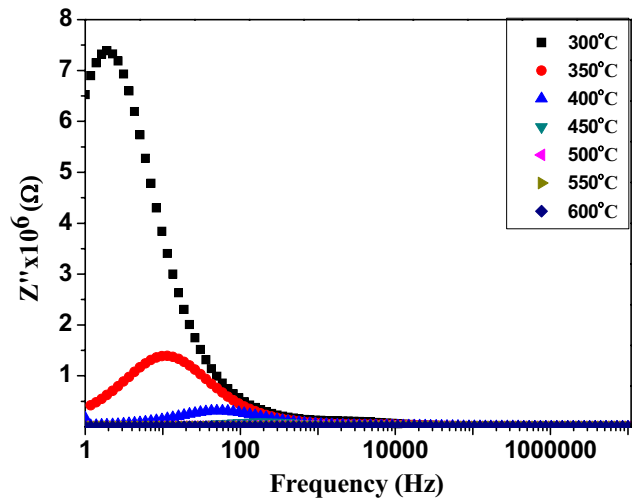

Fig. 4 Variation of imaginary part of impedance (Z'') with frequency measured at different temperatures for $BaZr_{0.05}Ti_{0.95}O_3$ ceramic

relaxation process is due to the presence of immobile species at lower temperatures and defects/vacancies at higher temperatures [49].

The variation of normalized parameter Z'/Z''_{max} as a function of logarithmic normalized frequency ($\log\omega/\omega_{max}$) at various temperatures is shown in Fig. 5, where ω_{max} corresponds to the frequency for Z''_{max}. As seen in the figure, different curves coalesce at one peak irrespective of the temperatures. This overlapping of curves corresponding to different Z'/Z''_{max} values indicates that the distribution of relaxation time is independent of temperature. The overlapping of peaks suggests the existence of both long range and localized relaxations in the system. In order to mobilize
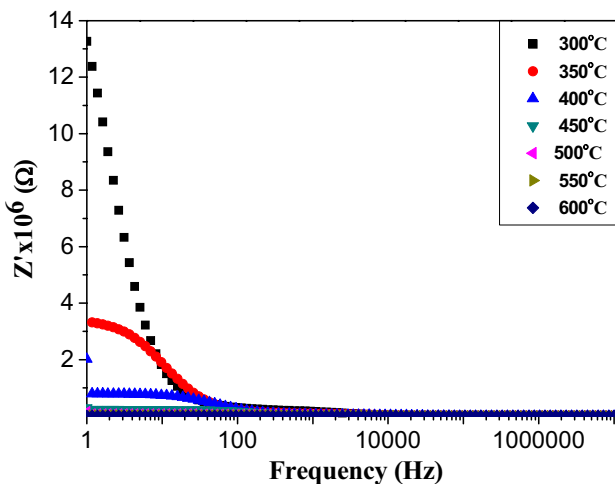

Fig. 3 Variation of real part of impedance (Z') with frequency measured at different temperatures for $BaZr_{0.05}Ti_{0.95}O_3$ ceramic
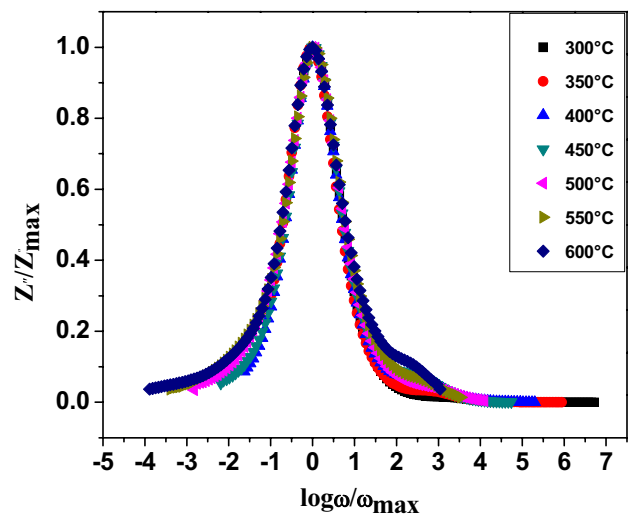

Fig. 5 Normalized parameters (Z''/Z''_{max}) versus $\log(\omega/\omega_{max})$ plots at different temperatures

the localized electron, the support of lattice vibrations is essential. In these circumstances, electrons are considered not to move by them, but by hopping motion activated by lattice oscillation. In addition, the magnitude of the activation energy suggests that the carrier transport is due to the hopping conduction.

The Nyquist plot or Cole–Cole plot is another important tool to study the relaxation and conduction processes. It helps to calculate different parameters associated with grain and grain boundary effects. Figure 6 represents the Nyquist plots for BZT ceramic plotted between Z′ and Z″ at different temperatures. The plot indicates that the area of the semicircle decreases as the temperature increases, highlighting decrease in resistivity with increasing temperature. Two depressed semicircles are observed representing the presence of both the grains and grain boundaries. The semicircle with high frequency corresponds to the contribution due to grains and the low frequency semicircle corresponds to the grain boundary effect [44]. In order to obtain the parameters regarding grains and grain boundaries, the experimental data are fitted to equivalent circuit.
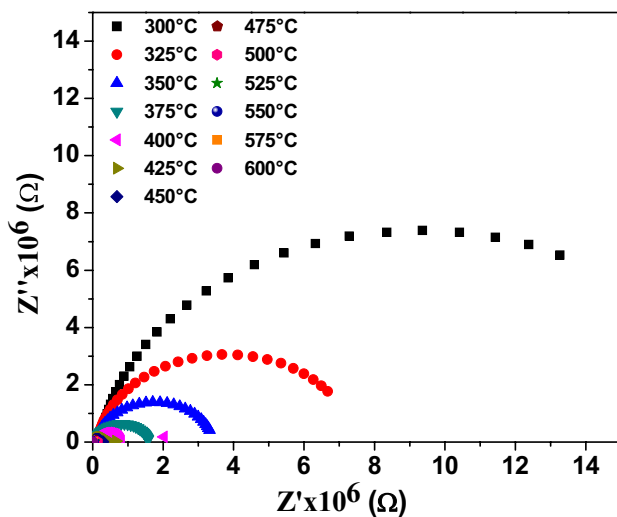

Fig. 6 Cole–Cole plots for $BaZr_{0.05}Ti_{0.95}O_3$ ceramic at different temperatures

The circuit is a combination of series of two parallel connected resistances and constant phase element (CPE). The fitting parameters are obtained by Zsimpwin software with modeled circuits. The experimental values of grain resistance (R_g) and grain boundary resistance (R_{gb}) at different temperatures obtained from the intercept of the semicircular arc on the real axis (Z″) are enlisted in Table 1. All the semicircles show some degree of depression instead of centered at the Z′ axis. This is due to the distribution of relaxation time. This type of relaxation in the system indicates the non-Debye type relaxation. This non ideal behavior (deviation from Debye's law) can be explained in terms of grain orientation, grain boundary, stress strain phenomenon and atomic defect distribution [50].

3.4 Electrical modulus studies

The complex dielectric modulus corresponds to the relaxation of the electric field in the material, when the electrical induction D is maintained as constant, and is defined by Eq. (3) [51, 52]. The values of real (M′) and imaginary (M″) components of the modulus are obtained from the following expressions:

$$M' = \omega C_0 Z'' \tag{7}$$

$$M'' = \omega C_0 Z' \tag{8}$$

Figure 7 depicts the frequency dependent variation of real part of electrical modulus (M′) at various temperatures. It is observed from the graph that the value of M′ in all the cases is almost zero at lower frequencies, which continuously increases with increasing frequency, and finally saturates at higher frequencies for all temperatures. This can be attributed to the presence of conduction phenomenon due to short-range mobility of charge carriers. Figure 8 shows frequency dependent variation of imaginary part of electrical modulus (M″) at various temperatures. It is observed that the peak value (M''_{max}) shifts towards higher frequency with increasing temperature. This indicates sharp dependence of M″ on temperature and frequency correlating the motion of mobile charge carriers. These curves reflect
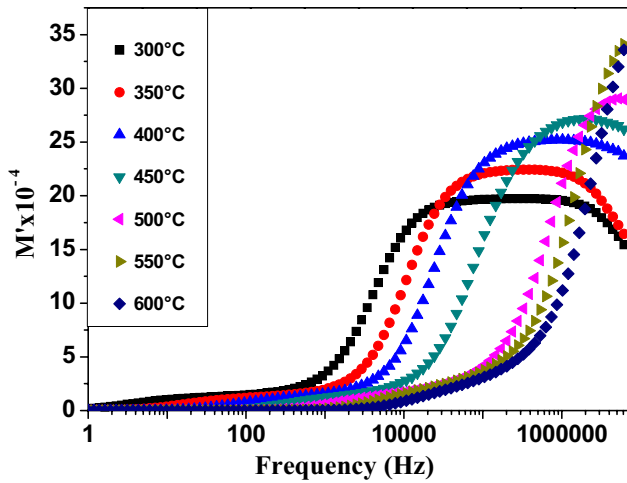
Table 1 Parameters obtained from temperature dependent impedance spectroscopy data of $BaZr_{0.05}Ti_{0.95}O_3$ ceramic

Temperature (°C)	R_g (KΩ)	R_{gb} (MΩ)	C_g (nF)	C_{gb} (nF)	τ_g (*10^{-5})	τ_{gb} (*10^{-3})
300	1714	17.98	0.3167	6.011	54.28	108.07
350	72.58	3.741	2.636	8.024	19.13	30.02
400	44.37	1.29	0.4324	7.359	1.91	9.49
450	10.23	0.218	5.195	8.032	5.3	1.75
500	1.39	0.066	2.115	2.322	0.29	1.53
550	0.77	0.045	0.189	1.92	0.01	0.086
600	0.51	0.009	0.1835	1.78	0.009	0.016

Fig. 7 Variation of real part of electrical modulus (M′) with frequency at different temperatures for BaZr$_{0.05}$Ti$_{0.95}$O$_3$ ceramic
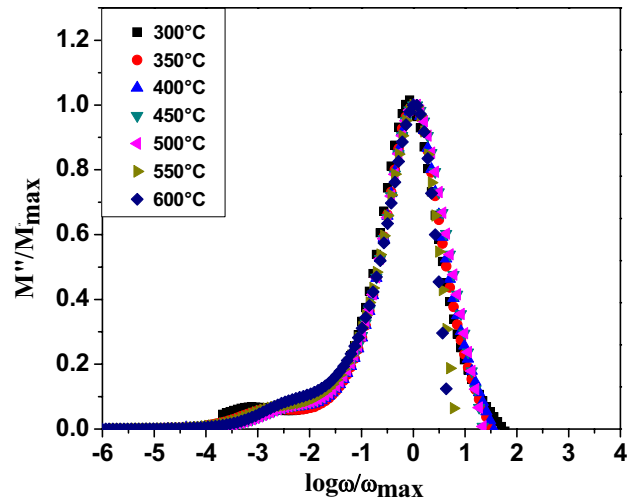

Fig. 9 Normalised parameters (M″/M″$_{max}$) versus log(ω/ω$_{max}$) plots at various temperatures for BaZr$_{0.05}$Ti$_{0.95}$O$_3$ ceramic

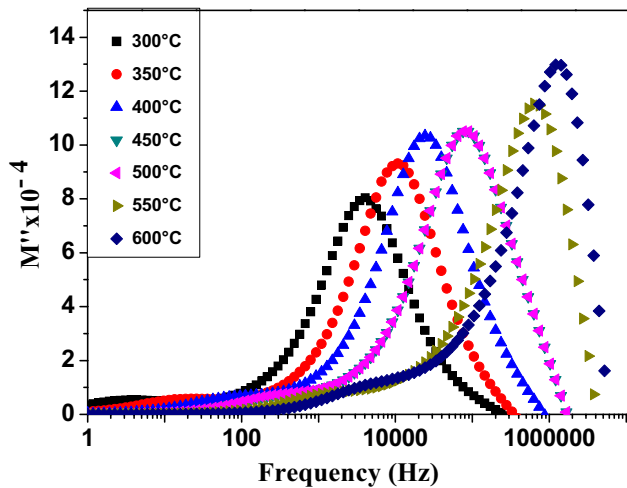**Fig. 8** Variation of imaginary part of electrical modulus (M″) with frequency at different temperatures for BaZr$_{0.05}$Ti$_{0.95}$O$_3$ ceramic

similar nature. The overlapping of data suggests the presence of both long range and localized relaxations in the system. The electrical modulus data allow the determination of defect relaxation or non-localized conduction, i.e. ionic or electronic conductivity. The low frequency part in Fig. 9 (left side) represents the range of frequencies in which charge carriers can move long distance and perform hopping from one site to other, while high frequency part (right side) represents the range of frequencies in which the charge carriers are confined to their potential wells and can make localized movements inside the well. The peak position in the graph indicates transition from long range to short range mobility [52]. Further, the coincidence of peaks for all the temperatures below a certain value of logω/ω$_{max}$ indicates temperature dependent relaxation process in the system.

3.5 Activation energy

The temperature dependent thermally activated processes are commonly expressed in terms of Arrhenius equation:

$$Z = A_0 \exp\left(\frac{-Ea}{RT}\right) \tag{9}$$

where A$_0$ is pre-exponential constant, E$_a$ is the activation energy, T is the absolute temperature (K) and R (8.31 Jmol^{-1}K^{-1}) is the universal gas constant. The Arrhenius plot between ln(Z) and 1000/T is usually used to determine the activation energy and pre-exponential term with the help of the slope and intercept, respectively. Figure 10 presents the Arrhenius plot drawn between log f and 10^3/T obtained from imaginary part of impedance (Z″) and electrical modulus (M″). The activation energy values

motion of ions in the material by exhibiting two apparent relaxation regions. The region on left side of the peak indicates the conduction process, while region on the right side of the peak is associated to the relaxation process where the ion can make localized motion within the well [53]. Also, the broadening of peaks is asymmetric in nature, which shows spread of relaxation time having different time constants (non-Debye type).

In order to study the scaling behavior of the sample at different temperatures, the normalized values of modulus (M″/M″$_{max}$) are plotted as a function of frequency (logω/ω$_{max}$) where ω$_{max}$ is the frequency corresponding to M″$_{max}$. Figure 9 shows the plot between M″/M″$_{max}$ and logω/ω$_{max}$ at elevated temperatures. A comparison between scaled impedance (Fig. 8) and scaled modulus (Fig. 9) resembles

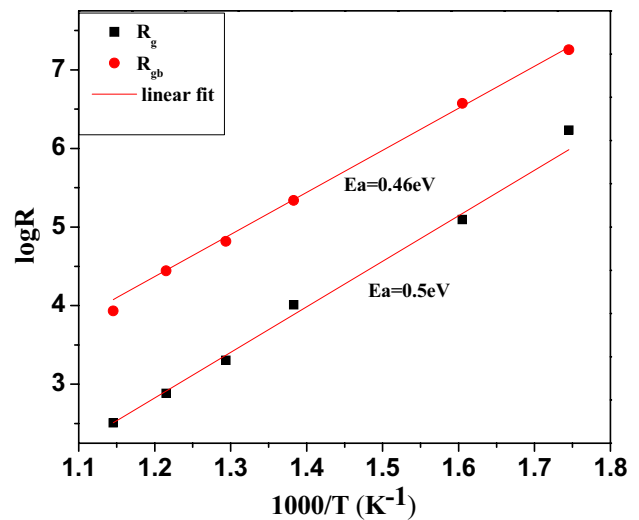**Fig. 10** Arrhenius plot between log f and 1000/T from Z″ and M″ for BaZr$_{0.05}$Ti$_{0.95}$O$_3$ ceramic

Fig. 12 Arrhenius plot of grain (R$_g$) and grain boundary (R$_{gb}$) resistance for BaZr$_{0.05}$Ti$_{0.95}$O$_3$ ceramic
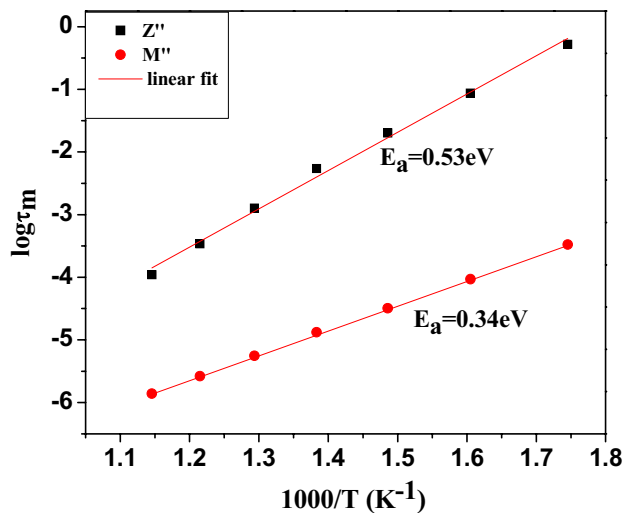

Fig. 11 Variation of relaxation time (logτ) with absolute temperature (1000/T) for BaZr$_{0.05}$Ti$_{0.95}$O$_3$ ceramic

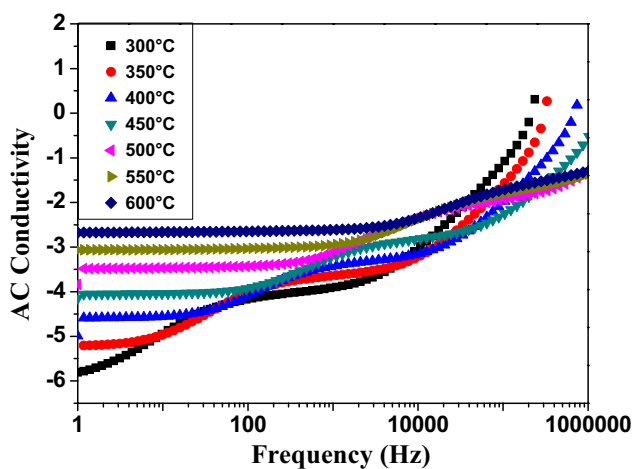**Fig. 13** Variation of AC conductivity of BaZr$_{0.05}$Ti$_{0.95}$O$_3$ ceramic with frequency at different temperatures

calculated from the linear fit of the graphs are found to be 0.52 and 0.53 eV for Z″ and M″, respectively. The most probable value of the relaxation frequency is determined using the relation $\omega_m \tau_m = 1$, where τ_m is the most probable relaxation time [54]. The linear fitting (Fig. 11) of the experimental data points is found to obey the Arrhenius law as given below:

$$\tau_m = \tau_0 \exp\left(-\frac{E_a}{KT}\right) \tag{10}$$

The grain resistance (logR$_g$) and grain boundary resistance (logR$_{gb}$) also follow the Arrhenius law, which

is illustrated in Fig. 12 and the estimated values of activation energies are also shown in the figure.

3.6 AC/DC conductivity

The bulk conductivity of a material is a thermally stimulated concept, which obeys Arrhenius law and can be evaluated from impedance plots using the relation:

$$\sigma_{ac} = \frac{Z'}{Z'^2 + Z''^2} \times \frac{t}{A} \tag{11}$$

where Z′ and Z″ are real and imaginary parts of impedance, t is the thickness of the pellet, and A is the area. The plots

of electrical conductivity (AC) as a function of frequency at different temperatures are illustrated in the Fig. 13. The graph mainly consists of three regions (i) low frequency dispersion (ii) moderate frequency (plateau) dispersion and (iii) high frequency conductivity dispersion with changing slopes. The variation of conductivity in the low frequency range is due to the polarization effect (space-charge). The frequency independent plateau at moderate frequency is attributed to the long-range translational motion of ions contributing to dc conductivity (σ_{dc}) [55]. The plots reveal that the conductivity of the material increases with increasing temperature. Also, at lower frequency side the dispersion is clearly visible, but the curves are found to merge at higher frequency. However, in high frequency region the conductivity increases for all the temperatures with changing slope. The frequency at which slope changes, is known as hopping frequency. As noticed from the figure, the hopping frequency shifts towards higher side with increasing temperature [56].

Figure 14 shows the variation of σ_{dc} with 1000/T. The value of bulk conductivity of the material is evaluated from ac conductivity plot of the sample at different temperatures by theoretical fitting using Jonscher's power law as given below [48]:

$$\sigma_{ac} = \sigma_{dc} + A\omega^n \tag{12}$$

where σ_{ac} is the AC conductivity, σ_{dc} is the limiting frequency conductivity, A is pre-exponential factor, ω is the angular frequency, and n is power law exponent falling between 0 and 1. At higher temperatures, the conductivity versus temperature response is almost a straight line and
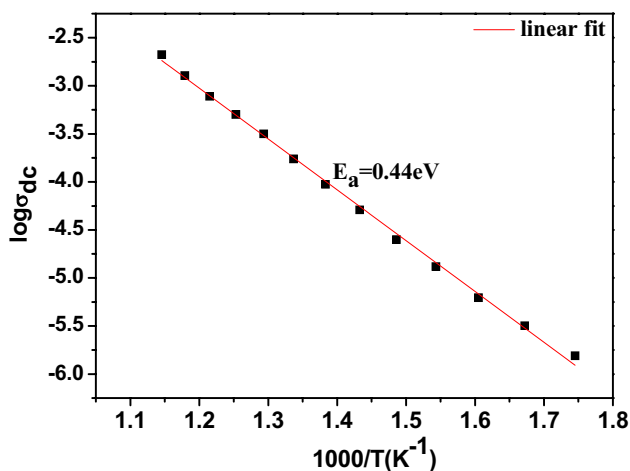
can be explained easily by thermally activated transport of Arrhenius type:

$$\sigma_{dc} = \sigma_0 \exp\left(\frac{-Ea}{KBT}\right) \tag{13}$$

where σ_0 is pre exponential factor, E_a is the activation energy of mobile charge carriers, K_B is the Boltzmann's constant and T is the absolute temperature. From the graph shown in Fig. 13, the dc activation energy of the sample is estimated to be 0.44 eV. The oxygen vacancies play very important role in the conduction process. In perovskite type ferroelectric materials, especially in titanates, oxygen vacancies are considered as the mobile charge carriers and the ionization of oxygen vacancies create conduction electrons according to the Kröger–Vink notation given as:

$$O_o^X \rightarrow \frac{1}{2}O_2 + V_o^{\blacksquare\blacksquare} + 2e^- \tag{14}$$

These excess electrons may be trapped by Ti^{4+} ions or oxygen vacancies, behave as conducting electrons during thermal agitation. The oxygen vacancies can be created due to three different charge states: (i) neutral state $\left(V_o^X\right)$, which is capable of capturing two electrons, mono ionized state $\left(V_O^{\blacksquare}\right)$ and double ionized state $\left(V_O^{\blacksquare\blacksquare}\right)$, which do not capture electrons. But, these two charge states are twofold positive and can be thermally activated, thus enhancing the conduction process.

4 Conclusions

The polycrystalline $BaZr_{0.05}Ti_{0.95}O_3$ ceramic was successfully prepared by SSRT. The XRD pattern confirmed the formation of pure phase with orthorhombic structure at room temperature having space group Amm2. SEM image revealed the growth of dense grains along with presence of ferroelectric domains. The frequency and temperature dependent impedance studies revealed NTCR behavior of BZT sample. The electric modulus studies indicated the existence of different relaxation times, which decrease with temperature obeying Arrhenius law. The distribution of relaxation time is found to be independent of temperature. The Nyquist plots highlight the decrease in resistivity with increasing temperature and establish the involvement of non-Debye type of relaxation in the system. The modulus studies signified the possibility of hopping mechanism in the charge transport process also. The activation energy values calculated from the linear fit of the graphs are found to be 0.52 and 0.53 eV for imaginary part of impedance and electrical modulus, respectively. The AC conductivity spectra were found to obey the Jonscher's power law. The

Fig. 14 Temperature dependence of dc conductivity for $BaZr_{0.05}Ti_{0.95}O_3$ ceramic. The *dots* are experimental points and line represents its linear fit

conduction process was observed to be thermally activated and followed Arrhenius law.

References

1. P. Kantha, K. Pengpat, P. Jarupoom, U. Intatha, G. Rujijanagul, T. Tunkasiri, Curr. Appl. Phys. **9**, 460–466 (2009)
2. C. Peng, J.F. Li, W. Gong, Mater. Lett. **59**, 1576–1580 (2005)
3. D. Lin, K.W. Kwok, H.L.W. Chan, Mater. Chem. Phys. **109**, 455–458 (2008)
4. H. Maiwa, Jpn. J. Appl. Phys. **46**, 7013 (2007)
5. Z. Zhang, J. Jia, H. Yang, C. Chen, H. Sun, X. Hu, D. Yang, J. Mater. Sci. **43**, 1501 (2008)
6. Z. Chen, J. Hu, Ceram. Inter. **35**, 111–115 (2009)
7. M.Z.C. Hu, V. Kurian, E.A. Payzant, C.J. Rawn, R.D. Hunt, Powder Technol. **110**(1), 2–14 (2000)
8. R.H. Upadhyay, A.P. Argekar, R.R. Deshmukh, Bull. Mater. Sci. **37**(3), 481–489 (2014)
9. Y. Wei, Y. Song, X. Deng, B. Han, X. Zhang, Y. Shen, Y. Lin, J. Mater. Sci. Technol. **30(8)** 743–747 2014
10. T.G. Reynolds, Am. Ceram. Soc. Bull. **80**, 29–32 (2001)
11. P.K. Patel, J. Rani, N. Adhlakha, H. Singh, K.L. Yadav, J. Phys. Chem. Solids **74**, 545–549 (2013)
12. S. Devi, A.K. Jha, Asian J. Chem. **21**(10), 117–124 (2009)
13. H. Kishi, Y. Mizuno, H. Chazono, Jpn. J. Appl. Phys. **42**, 1–15 (2003)
14. R.Z. Chen, A.L. Cui, X.H. Wang, L. Li, Mater. Sci. Eng. B **99**, 302–305 (2003)
15. J.F. Chen, Z.G. Shen, F.T. Liu, X.L. Liu, J. Yun, Scr. Mater. **49**, 509–514 (2003)
16. K. Uchino, *Ferroelectric Devices* (Marcel Dekker, New York, 2000)
17. Z. Yu, C. Ang, R. Guo, A.S. Bhalla, Mater. Lett. **61**, 326–329 (2007)
18. F. Moura, A.Z. Simo̴es, B.D. Stojanovic, M.A. Zaghete, E. Longo, J.A. Varela, J. Alloys Compd. **462**, 129–134 (2008)
19. C.E. Ciomaga, V. Massimo, M.T. Buscaglia, V. Buscaglia, L. Mitoseriu, A. Stancu, P. Nanni, J. Eur. Ceram. Soc. **27**, 4061–4064 (2007)
20. J.W. Zhai, X. Yao, L.Y. Zhang, B. Shen, Appl. Phys. Lett. **84**, 3136–3138 (2006)
21. Z.Y. Cheng, R.S. Katiyar, X. Yao, A.S. Bhalla, Phys. Rev. B **57**, 8166–8177 (1998)
22. A.K. Kalyani, A. Senyshyn, R. Ranjan, J. Appl. Phys. **114**(1–6), 014102 (2013)
23. Z.G. Ye, *Handbook of Advanced Dielectric, Piezoelectric and Ferroelectric Materials*. (Woodhead Publishing Limited, Cambridge, 2008)
24. T. Badapanda, J. Adv. Ceram. **3(4)** 339–348 (2014)
25. T. Badapanda, S. Sarangi, B. Behera, S. Anwar, Curr. Appl. Phys. **14**, 1192–1200 (2014)
26. T. Badapanda, S.K. Rout, L.S. Cavalcante, J.C. Sczancoski, S. Panigrahi, E. Longo, M. Siu Li, J. Phys. D: Appl. Phys. **42**, 175414 (2009)
27. B. Garbarz-Glos, W. Bąk, M. Antonova, A. Budziak, K. Bormanis, C. Kajtoch, Ferroelecrrics **485**(1), 173–178 (2015)
28. T. Badapanda, S.K. Rout, S. Panigrahi, Ferroelectrics **385**, 6177–6186 (2009)
29. A. Dixit, S.B. Majumder, A. Savvinov, R.S. Katiyar, R. Guo, A.S. Bhalla, Mater. Lett. **56**(6), 933–940 (2002)
30. X. Chou, J. Zhai, H. Jiang, X. Yao, J. Appl. Phys. **102**, 084106-1-084106-6 (2007)
31. Y. Hotta, G.W.J. Hassink, T. Kawai, H. Tabata, Jpn. J. Appl. Phys. **42**, 5908 (2003)
32. Y. Zhi, R. Guo, A.S. Bhalla, J. Appl. Phys. **88**, 410–415 (2000)
33. T. Hino, M. Nishida, T. Araki, T. Ohno, T. Kawahara, M. Murasugi, J. Laser Micro/Nanoeng. **2**, 166–169 (2007)
34. Y. Zhi, C. Ang, Z. Jing, R. Guo, A.S. Bhalla, J. Appl. Phys. **92**, 1489–1493 (2002)
35. B. Garbarz-Glos, W. Bąk, M. Antonova, M. Pawlik, Mat. Sci. Eng. **49**, 012031 (2013)
36. S. Sen, R.N.P. Choudhary, A. Tarafdar, P. Pramanik, J. Appl. Phys. **99**(12), 124114-1-124114-8 (2006)
37. N. Hannachi, I. Chaabane, K. Guidara, A. Bulou, F. Hiel, Mater. Sci. Eng. B **172**, 24–32 (2010)
38. L.P. Curecheriu, R. Frunza, A. Ianculescu, Appl. Ceram. **2**, 81–88 (2008).
39. X.L. Deng, D.J. Guo, W. Cai, C.L. Fu, Adm. Mater. Res. **412**, 86–89 (2011)
40. T. Badapanda, S. Sarangi, B. Behera, S. Parida, S. Saha, T.P. Sinha, R. Ranjan, P.K. Sahoo. J. Alloys Compd. **645**, 586–596 (2015)
41. Y. Tan, J. Zhang, Y. Wu, C. Wang, V. Koval, B. Shi, H. Ye, R. McKinnon, G. Viola, H. Yan, Sci. Rep. **5**(1–9), 9953 (2015)
42. B. Behera, P. Nayak, R.N.P. Choudhary, J. Alloys Compd. **436**, 226–232 (2007)
43. P. Jha, A.K. Jha, Bull. Mater. Sci. **36**(1), 135–141 (2013)
44. P. Ganguly, A.K. Jha, K.L. Deori, Solid State Commun. **146**, 472–477 (2008)
45. P. Sateesh, J. Omprakash, G.S. Kumar, G. Prasad, J. Adv. Dielectr. **5**(1), 1550002-1-1550002-13 (2015)
46. A. Kumar, B.P. Singh, R.N.P. Choudhary, A.K. Thakur, Mater. Chem. Phys. **99**, 150–159 (2006)
47. Q.K. Muhammad, M. Waqar, M.A. Rafiq, M.N. Rafiq, M. Usman, M.S. Anwar, J. Mater. Sci. **51**(22), 10048–10058 (2016)
48. J.R. Macdonald, W.B. Johnson, Fundamentals of impedance spectroscopy. in *Impedance Spectroscopy: Theory, Experiment, and Applications*, 2nd ed. (Wiley, Newark, 2005), pp. 1–26
49. B. Tiwari, R.N.P. Choudhary, J. Phys. Chem. Solids **69**(11), 2852–2857 (2008)
50. S. Sen, R.N.P. Choudhary, P. Pramanik, Phys. B **387**, 56–62 (2007)
51. A. Elbasset, F. Abdi, T. Lamcharfi, S. Sayouri, L.H. Omari, P. Bourson, A. Salhi, A. Elghandouri, Int. Rev. Phys. **8**(5), 141–149 (2014)
52. P.S. Das, P.K. Chakraborty, B. Behera, R.N.P. Choudhary, Phys. B **395**, 98–103 (2007)
53. R. Jacob, H.G. Nair, J. Isac, Proc. Appl. Ceram. **9**(2), 73–79 (2015)
54. T. Badapanda, R.K. Harichandan, S.S. Nayak, A. Mishra, S. Anwar, Proc. Appl. Ceram. **8**(3), 145–153 (2014)
55. W. Li, R.W. Schwartz, Appl. Phys. Lett. **89**, 242906 (2006)
56. K. Srinivas, P. Sarah, S.V. Suryanarayana, Bull. Mater. Sci. **26**, 247–253 (2003)